# A membrane theory for circular graphene sheets, based on a hyperelastic material model for large deformations

Raphael Höller , Florian Libisch & Christian Hellmich

View supplementary material

Published online: 20 Jul 2020.

Submit your article to this journal

Article views: 226

View related articles

View Crossmark data

Taylor & Francis
Taylor & Francis Group

ORIGINAL ARTICLE

OPEN ACCESS

Check for updates

# A membrane theory for circular graphene sheets, based on a hyperelastic material model for large deformations

Raphael Höller[a], Florian Libisch[b], and Christian Hellmich[a]

[a]Institute for Mechanics of Materials and Structures, TU Wien – Vienna University of Technology, Vienna, Austria; [b]Institute for Theoretical Physics, TU Wien – Vienna University of Technology, Vienna, Austria

## ABSTRACT

Large deflections relevant for suspended circular graphene sheets with simply supported boundaries are computed by a theory for 2D membranes subjected to several types of vertical axisymmetric forces, based on the principle of virtual power (PVP). Corresponding stress–strain relations are provided in the form of a nonlinear hyperelastic material model for graphene. When approximating the deflections through Fourier series, the PVP yields a nonlinear algebraic system of equations, which is solved by the iterative Newton–Raphson procedure. The new computational efficient method is validated through comparison of the numerical results it provides, with predictions obtained from experimental nanoindentaion measurements.

## 1. Introduction

Two-dimensional (2D) graphene membranes, consisting of carbon atoms arranged in a hexagonal lattice, attract considerable attention in the fields of chemistry, physics, and material science [1–5]. As regards membrane theories for computing the deflections of suspended graphene sheets, several methods have been used up to the present day: Atomistic models of graphene membranes have been developed by molecular dynamics simulations using interatomic Lennard–Jones potentials and Tersoff–Brenner potentials [6–9], as well as by truss-type models consisting of beam elements for simulating covalently bonded carbon atoms in a hexagonal graphene lattice [10–12]. The by far most popular method for the solution of mechanical deformations is that of the finite element method, which has been the basis for many scientific contributions up to the present day [13–21]. Besides mechanical deformations, vibrational analysis of graphene sheets was performed indicating its fundamental frequencies and mode shapes [19, 22–24].

However, for a circular graphene membrane, simply supported at its boundary, a more computationally efficient Fourier series-based theory can be provided: Therefore, we resort to the principle of virtual power (PVP) [25–33], which we specify for the kinematic characteristics of a 2D graphene membrane in bending mode, see Section 2. In this context, we consider large deformations using Lagrangian quantities, namely the Green–Lagrange strain and the energetically conjugated second Piola–Kichhoff stress. Corresponding stress--strain relations are linked by a nonlinear, anisotropic

hyperelastic material model of graphene [34], based on density functional theory (DFT) [35, 36]. Furthermore, the investigated circular membranes are subjected to several types of axisymmetric vertical forces, namely to single forces or to distributed surface loads acting on circular areas, whereby the action points and the areas form axisymmetric patterns. Such kinds of concentrated loads allow for consideration of nanoindentation of free-standing graphene membranes [3]. In Section 3, the PVP-based governing equation is used for constructing a nonlinear algebraic system of equations for determining the sought deflection function. The latter is expanded into Fourier series according to Navier's proposal [37] and the unknown Fourier coefficients of the nonlinear multivariate system of equations are determined iteratively using the Newton–Raphson method [38]. Section 4 is devoted to numerical investigations in the form of three representative examples, and to comparing respective results with experimental measurements. Finally, concluding remarks are provided in Section 5. Appendix A contains the algebraic system of equations for the three aforementioned numerical examples, in order to solve the unknown Fourier coefficients.

## 2. Kinematics and stress resultants of suspended graphene membranes for large deformations – reviewed in the context of the PVP
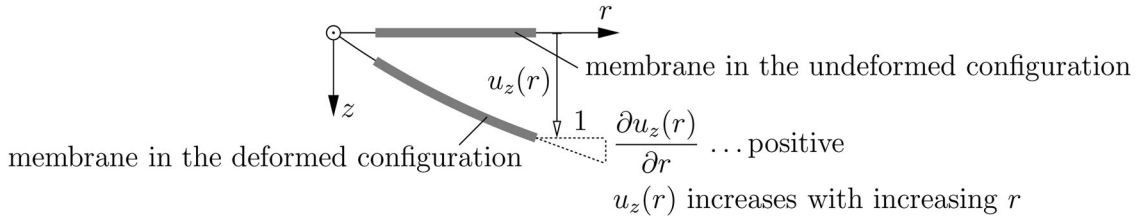
### 2.1. Basics

The PVP is an efficient and safe method for constructing energetically consistent theories of structural members, as

**Figure 1.** Sideview in the *r–z*-plane of a graphene membrane in the undeformed and in the deformed configuration.

documented by [25–27] and [29, 30]. Setting our focus point on 2D graphene membranes, we start with the formulation of the PVP for a standard 3D continuum, in the format put forward by Germain and followers [30–33,39],

$$\mathcal{P}^{ext} + \mathcal{P}^{int} = 0, \tag{1}$$

with

$$\mathcal{P}^{ext} = + \int_V \mathbf{f}(\mathbf{x}) \cdot \hat{\mathbf{v}}(\mathbf{x}) \; dV + \int_S \mathbf{T}(\mathbf{n}, \mathbf{x}) \cdot \hat{\mathbf{v}}(\mathbf{x}) \; dS, \tag{2}$$

$$\mathcal{P}^{int} = - \int_V \boldsymbol{\sigma} : \hat{\mathbf{d}} \; dV, \tag{3}$$

where $\mathcal{P}^{ext}$ and $\mathcal{P}^{int}$ denote the virtual power of the external forces and of the internal forces, respectively; $\mathbf{x}$ denotes the actual location vectors throughout the continuum and at its boundaries with outward normals $\mathbf{n}$; $\mathbf{f}$ denotes volume forces; $\mathbf{T}$ denotes traction (surface) forces; $\hat{\mathbf{v}}$ denotes the virtual velocity; $\boldsymbol{\sigma}$ denotes the Cauchy stress; and $\hat{\mathbf{d}}$ denotes the virtual Eulerian strain rate. The PVP implies both kinematic compatibility and equilibrium of the solid continuum.

In the case of circular membranes, undergoing large deformations, we formulate strains and stresses as a function of the location vector $\mathbf{X}$ in the undeformed configuration (Lagrangian representation). Any position within the surface of such a membrane is described by a cylindrical coordinate system, with an origin located in the center of the membrane, and with base vectors $\mathbf{e}_r, \mathbf{e}_\varphi$, and $\mathbf{e}_z$. The latter is orthogonal to the undeformed membrane and the azimuth of $\varphi = 0$ corresponds to a base vector $\mathbf{e}_r$ pointing in the so-called "zigzag" direction of graphene. Thus, for describing large deformations, the following virtual power of external and internal forces are provided in Lagrangian representation

$$\mathcal{P}^{ext} = \int_0^R \int_0^{2\pi} \hat{\mathbf{v}}(\mathbf{X}) \cdot \mathbf{F} \cdot \boldsymbol{\pi}(\mathbf{X}) \cdot \mathbf{N}(\mathbf{X}) \; r \, d\varphi \, dr, \tag{4}$$

$$\mathcal{P}^{int} = - \int_0^R \int_0^{2\pi} \int_{-\frac{h}{2}}^{+\frac{h}{2}} \boldsymbol{\pi} : \dot{\hat{\mathbf{E}}} \; r \, dz \, d\varphi \, dr, \tag{5}$$

where $\mathbf{X}$ denotes the initial location vectors throughout the membrane with outward normals $\mathbf{N}$ and radius $R$; $\mathbf{F}$ denotes the deformation gradient; $\boldsymbol{\pi}$ denotes the second Piola–Kirchhoff stress tensor; and $\dot{\hat{\mathbf{E}}}$ denotes the virtual Green–Lagrange strain rate. Note that we neglected volume force vectors due to the infinitesimal small thickness of graphene (single layer of carbon atoms), see Section 2.2.

## 2.2. Kinematics

2D graphene membranes in so-called bending mode are characterized by the following kinematic features:

1. The thickness of graphene is negligibly *small* [4, 5], such that all straight lines (generators) orthogonal to the undeformed membrane remain, throughout the deformation process, *straight*, constant in length, and *orthogonal* to the undeformed membrane plane.
2. All points of a generator have, in good approximation, the same displacement in the *z*-direction, namely the deflection $u_z$, see Figure 1.
3. The deflections are *large* when compared to the thickness of the membrane.
4. Axisymmetric loads result in axisymmetric patterns of the displacements.
5. Stretching stiffness is dominant over negligible shear and bending stiffnesses.

Under the aforementioned kinematic conditions, the displacement field of the membrane reads as

$$\mathbf{u}(\mathbf{X}) = u_z(r) \; \mathbf{e}_z, \tag{6}$$

and the corresponding virtual velocity field follows from a virtual displacement field of the form

$$\hat{\mathbf{u}}(\mathbf{X}) = \hat{u}_z(r) \; \mathbf{e}_z. \tag{7}$$

Namely, temporal derivation of (7) yields the virtual velocity field as

$$\hat{\mathbf{v}}(\mathbf{X}) = \dot{\hat{\mathbf{u}}}(\mathbf{X}) = \hat{v}_z(r) \; \mathbf{e}_z, \tag{8}$$

with $\hat{v}_z$ as the temporal derivative of the time-dependent virtual displacement $\hat{u}_z$.

Displacement field (6) implies a Green–Lagrange strain tensor $\mathbf{E}$ [32]

$$\mathbf{E} = \frac{1}{2} \left[ \frac{\partial \mathbf{u}}{\partial \mathbf{X}} + \left( \frac{\partial \mathbf{u}}{\partial \mathbf{X}} \right)^T + \left( \frac{\partial \mathbf{u}}{\partial \mathbf{X}} \right)^T \cdot \frac{\partial \mathbf{u}}{\partial \mathbf{X}} \right]$$

$$= \sum_{i=r,\varphi,z} \sum_{j=r,\varphi,z} E_{ij} \; \mathbf{e}_i \otimes \mathbf{e}_j, \tag{9}$$

with non-zero components reading as

$$E_{rr}(r) = \frac{1}{2} \left( \frac{\partial u_z(r)}{\partial r} \right)^2, \tag{10}$$

where the transverse shear strains are neglected due to the extreme thinness of the 2D membrane. Derivation of (10) with respect to the time, and substitution of the occurring time derivatives of displacements by virtual velocities, yields

$$\dot{\hat{\mathbf{E}}} = \dot{\hat{E}}_{rr} \ \mathbf{e}_r \otimes \mathbf{e}_r, \tag{11}$$

with

$$\dot{\hat{E}}_{rr}(r) = \frac{\partial u_z(r)}{\partial r} \ \frac{\partial \hat{v}_z(r)}{\partial r}. \tag{12}$$

Thus, the virtual Green–Lagrange strain rate (appearing in the virtual power of internal forces) depends on both the virtual velocity $\hat{v}_z$ and the actual deflection $u_z$ indicating a non-linearity in the structural problem.

Furthermore, displacement field (6) implies a deformation gradient, $\mathbf{F} = \mathbf{1} + \partial \mathbf{u}/\partial \mathbf{X}$ (appearing in the virtual power of external forces), reading as

$$\mathbf{F} = F_{rr} \ \mathbf{e}_r \otimes \mathbf{e}_r + F_{\varphi\varphi} \ \mathbf{e}_\varphi \otimes \mathbf{e}_\varphi + F_{zr} \ \mathbf{e}_z \otimes \mathbf{e}_r + F_{zz} \ \mathbf{e}_z \otimes \mathbf{e}_z, \tag{13}$$

with

$$F_{rr} = 1, \quad F_{\varphi\varphi} = 1, \quad F_{zr} = \frac{\partial u_z(r)}{\partial r}, \quad \text{and} \quad F_{zz} = 1. \tag{14}$$

## 2.3. Virtual power of internal forces and corresponding hyperelastic material model of graphene

As regards specification of the virtual power of internal forces (5) for the kinematic characteristics of graphene membranes undergoing large deformations, the virtual Green–Lagrange strain rates (12) imply that only stresses $\pi_{rr}$ perform power along the virtual strain rates $\dot{\hat{E}}_{rr}$. Hence, the virtual power of the internal forces reads as

$$\mathcal{P}^{int} = -\int_0^R \int_0^{2\pi} \int_{-\frac{h}{2}}^{+\frac{h}{2}} \pi_{rr}(r) \ \dot{\hat{E}}_{rr}(r) \ r \, dz \, d\varphi \, dr$$

$$= -\int_0^R \int_0^{2\pi} \int_{-\frac{h}{2}}^{+\frac{h}{2}} \pi_{rr}(r) \left[ \frac{\partial u_z(r)}{\partial r} \ \frac{\partial \hat{v}_z(r)}{\partial r} \right] r \, dz \, d\varphi \, dr. \tag{15}$$

Equation (15) indicates that the membrane-specific "degrees of freedom" $\frac{\partial u_z(r)}{\partial r} \frac{\partial \hat{v}_z(r)}{\partial r}$ induce internal stress resultants on which they produce power, namely internal forces per unit length

$$n_{L,rr}(r) = \int_{-\frac{h}{2}}^{+\frac{h}{2}} \pi_{rr}(r) \ dz \equiv \pi_{rr}^{2D}(r). \tag{16}$$

Stress resultant (16) can be interpreted as the normal component of the 2D second Piola–Kirchhoff stress tensor in $\mathbf{e}_r$ direction acting on a 2D solid. For a hexagonal graphene lattice, the nonlinear, anisotropic material behavior is described by the following hyperelastic stress–strain relation [34]

$$n_{L,rr} = \rho_{m,0}^{2D} [\beta_1 + \beta_2 \ E_{rr} + \beta_3 \ S_{rr}]. \tag{17}$$

In Eq. (17), $\rho_{m,0}^{2D}$ is the initial mass density per area of graphene; $\beta_1$, $\beta_2$, and $\beta_3$ are scalars depending on graphene's DFT-based material fitting coefficients $c_i$ and principal invariants $I_i$ of the strain and structural tensor [34][1]

$$\begin{aligned} \beta_1 &= c_2 \ I_1 + c_6 \ I_1^2 + c_9 \ I_1^3 + c_{13} \ I_3, \\ \beta_2 &= -c_2 + 2 \ c_4 + (3 \ c_5 - c_6)I_1 + (4 \ c_7 - c_9)I_1^2, \\ \beta_3 &= c_3 + c_{13} \ I_1, \end{aligned} \tag{18}$$

with

$$I_1 = E_{rr}, \quad I_3 = E_{rr}^3 \ \cos(6\varphi). \tag{19}$$

$S_{rr}$ refers to the anisotropic behavior and is the component of the second-order tensor, $\mathbf{S} = \partial I_3 / \partial \mathbf{E}$, reading as,

$$S_{rr} = 3 \ E_{rr}^2 \cos(6\varphi), \tag{20}$$

characterizing the influence of the strain of $E_{rr}$ onto the mechanical response of graphene.

Inserting (16) together with (17)–(19) into the power expression (15) yields the virtual power of internal forces in the following form

$$\mathcal{P}^{int} = -\rho_{m,0}^{2D} \int_0^R \int_0^{2\pi} \Big[ 2 c_4 E_{rr} + 3(c_5 + c_3 \cos(6\varphi))E_{rr}^2$$

$$+ 4(c_7 + c_{13} \cos(6\varphi))E_{rr}^3 \Big] \times \left[ \frac{\partial u_z(r)}{\partial r} \frac{\partial \hat{v}_z(r)}{\partial r} \right] r \, d\varphi \, dr. \tag{21}$$

Substitution of the Green–Lagrange strain (10) results in

$$\mathcal{P}^{int} = -\rho_{m,0}^{2D} \int_0^R \int_0^{2\pi} \Bigg[ c_4 \left( \frac{\partial u_z(r)}{\partial r} \right)^2 + \frac{3}{4} (c_5 + c_3 \cos(6\varphi)) \left( \frac{\partial u_z(r)}{\partial r} \right)^4$$

$$+ \frac{1}{2} (c_7 + c_{13} \cos(6\varphi)) \left( \frac{\partial u_z(r)}{\partial r} \right)^6 \Bigg] \times \left[ \frac{\partial u_z(r)}{\partial r} \frac{\partial \hat{v}_z(r)}{\partial r} \right] r \, d\varphi \, dr. \tag{22}$$

## 2.4. Virtual power of external forces and formulation of the PVP

Evaluating (4) for a membrane with outward normals $\mathbf{N} = \mathbf{e}_z$, with virtual velocity (8) and deformation gradient (13) and (14) yields

$$\mathcal{P}^{ext} = +\int_0^R \int_0^{2\pi} \hat{\mathbf{v}}(\mathbf{X}) \cdot \mathbf{F} \cdot \boldsymbol{\pi}(\mathbf{X}) \cdot \mathbf{e}_z \, r \, d\varphi \, dr$$

$$= +\int_0^R \int_0^{2\pi} \hat{v}_z(r) \cdot \left( \pi_{zz}(r) + \frac{\partial u_z(r)}{\partial r} \pi_{rz}(r) \right) r \, d\varphi \, dr. \tag{23}$$

Eq. (23) indicates that the membrane-specific degree of freedom $\hat{v}_z(r)$ induces external Lagrangian stress resultants on which power is produced, namely vertical Lagrangian surface loads (dimension force per unit area), reading as

---

[1]The fitting coefficients within the used hyperelastic material model of graphene are valid for Green–Lagrange strains between $-0.03$ and $+0.28$ [34, Table 2].
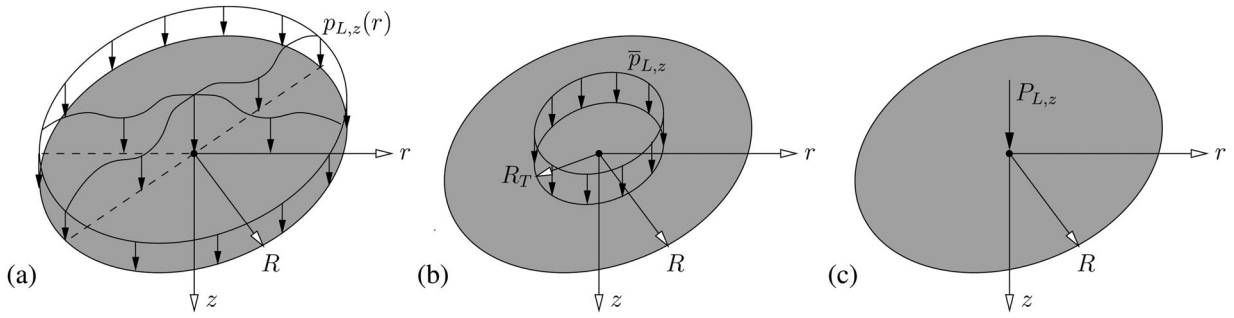
**Figure 2.** (a) Vertical surface load $p_{L,z}(r)$ non-uniformly distributed over the entire membrane; (b) vertical surface load $\bar{p}_{L,z}$ uniformly distributed over a centered circular area of radius $R_T$; and (c) vertical single force $P_{L,z}$ acting in the center of the membrane.

$$p_{L,z}(r) = \pi_{zz}(r) + \frac{\partial u_z(r)}{\partial r} \pi_{rz}(r). \tag{24}$$

Substitution of (24) into the power expression (23) yields the virtual power of external forces in the following form

$$\mathcal{P}^{ext} = + \int_0^R \int_0^{2\pi} p_{L,z}(r)\ \hat{v}_z(r)\ r\ d\varphi\ dr. \tag{25}$$

Regarding more complex loading cases, Eq. (25) can be straightforwardly extended to membranes loaded by surface loads per unit area $p_{L,z}(r)$ over the entire membrane, distributed forces $\bar{p}_{L,z}$ over the centered circular area of radius $R_T$, and vertical single forces $P_{L,z}$ acting at the center of the membrane, see Figure 2. In this context, the virtual power of external forces for a circular membrane subjected to axisymmetric loads reads as

$$\mathcal{P}^{ext} = + \int_0^R \int_0^{2\pi} p_{L,z}(r) \hat{v}_z(r) r\, d\varphi\, dr + \bar{p}_{L,z} \int_0^{R_T} \int_0^{2\pi} \hat{v}_z(r) r\, d\varphi\, dr$$
$$+ P_{L,z} \hat{v}_z(r) \Big|_{r=0}. \tag{26}$$

Insertion of the expression for the virtual power of internal forces (22) as well as of the expression for the virtual power of external forces (26), into the PVP (1), yields

$$\mathcal{P}^{ext} + \mathcal{P}^{int}$$
$$= + \int_0^R \int_0^{2\pi} p_{L,z}(r)\, \hat{v}_z(r)\, r\, d\varphi\, dr + \bar{p}_{L,z} \int_0^{R_T} \int_0^{2\pi} \hat{v}_z(r)\, r\, d\varphi\, dr + P_{L,z}\, \hat{v}_z(r)\Big|_{r=0}$$
$$- \rho_{m,0}^{2D} \int_0^R \int_0^{2\pi} \left[ c_4 \left( \frac{\partial u_z(r)}{\partial r} \right)^2 + \frac{3}{4}(c_5 + c_3 \cos(6\varphi)) \left( \frac{\partial u_z(r)}{\partial r} \right)^4 \right.$$
$$\left. + \frac{1}{2}(c_7 + c_{13} \cos(6\varphi)) \left( \frac{\partial u_z(r)}{\partial r} \right)^6 \right] \times \left[ \frac{\partial u_z(r)}{\partial r} \frac{\partial \hat{v}_z(r)}{\partial r} \right] r\, d\varphi\, dr = 0. \tag{27}$$

The PVP (27) is the basis for determining the unknown deflection function $u_z(r)$. We therefore expand the latter into a Fourier series, which leads to the so-called Galerkin method, as described in Section 3.

## 3. Mathematical solution procedure

The PVP in the form (27) can also be used for constructing a *nonlinear* algebraic system of equations giving access to the deflection function $u_z(r)$. For this purpose, we resort to Navier [37], representing the axisymmetric deflection function as a series of trigonometric functions, that is, a Fourier series

$$u_z(r) = \sum_{m=1}^{N_m} a_m\ w_m(r), \tag{28}$$

where $a_m$ are unknown Fourier coefficients (amplitudes), and $w_m$ denote corresponding trigonometric functions reading as

$$w_m(r) = \cos\left( \frac{m\, r\, \pi}{2\, R} \right) \quad \text{for} \quad m = 1, 3, 5... \tag{29}$$

Subscripts $m$ refer to the number of waves related to the trigonometric functions, with $N_m$ as the total number of employed deflection modes. Eq. (29) automatically ensures a circular membrane with simply supported boundaries, that is, deflection modes are zero for $r = R$: $w_m(R) = 0$.

Similar choices are made for the virtual velocities $\hat{v}_z(r)$, through introduction of ansatz functions identical to those in Eq. (28),

$$\hat{v}_z(r) = \sum_{t=1}^{N_t} \dot{\hat{a}}_t\ w_t(r), \tag{30}$$

with the virtual velocity coefficient $\dot{\hat{a}}_t$. Insertion of (28) and (30) into Eq. (27) yields the following Galerkin-type solution scheme

$$\mathcal{P}^{ext} + \mathcal{P}^{int}$$
$$= \sum_{t=1}^{N_t} \dot{\hat{a}}_t \left\{ \int_0^R \int_0^{2\pi} p_{L,z}\, w_t\, r\, d\varphi\, dr + \bar{p}_{L,z} \int_0^{R_T} \int_0^{2\pi} w_t\, r\, d\varphi\, dr + P_{L,z}\, w_t \Big|_{r=0} \right.$$
$$- \rho_{m,0}^{2D} \int_0^R \int_0^{2\pi} \left[ c_4 \left( \sum_{m=1}^{N_m} a_m \frac{\partial w_m}{\partial r} \right)^2 + \frac{3}{4}(c_5 + c_3 \cos(6\varphi)) \left( \sum_{m=1}^{N_m} a_m \frac{\partial w_m}{\partial r} \right)^4 \right.$$
$$\left. + \frac{1}{2}(c_7 + c_{13} \cos(6\varphi)) \left( \sum_{m=1}^{N_m} a_m \frac{\partial w_m}{\partial r} \right)^6 \right] \times \left( \sum_{m=1}^{N_m} a_m \frac{\partial w_m}{\partial r} \right) \frac{\partial w_t}{\partial r} r\, d\varphi\, dr \right\}$$
$$= 0. \tag{31}$$

After simplification, we further obtain a more suitable solution scheme

$$\mathcal{P}^{ext} + \mathcal{P}^{int}$$

$$= \sum_{t=1}^{N_t} \dot{\hat{a}}_t \left\{ \int\limits_0^R \int\limits_0^{2\pi} p_{L,z}\, w_t\, r\, d\varphi\, dr + \bar{p}_{L,z} \int\limits_0^{R_T} \int\limits_0^{2\pi} w_t\, r\, d\varphi\, dr + P_{L,z}\, w_t \Big|_{r=0} \right.$$

$$- 2\pi\, \rho_{m,0}^{2D}\, c_4 \sum_{j,k,l=1}^{N_m} a_j\, a_k\, a_l \int\limits_0^R \frac{\partial w_j}{\partial r} \frac{\partial w_k}{\partial r} \frac{\partial w_l}{\partial r} \frac{\partial w_t}{\partial r}\, r\, dr$$

$$- \frac{3}{2}\, \pi\, \rho_{m,0}^{2D}\, c_5 \sum_{j,k,l,m,n=1}^{N_m} a_j\, a_k\, a_l\, a_m\, a_n \int\limits_0^R \frac{\partial w_j}{\partial r} \frac{\partial w_k}{\partial r} \frac{\partial w_l}{\partial r} \frac{\partial w_m}{\partial r} \frac{\partial w_n}{\partial r} \frac{\partial w_t}{\partial r}\, r\, dr$$

$$\left. - \pi\, \rho_{m,0}^{2D}\, c_7 \sum_{j,k,l,m,n,q,s=1}^{N_m} a_j\, a_k\, a_l\, a_m\, a_n\, a_q\, a_s \int\limits_0^R \frac{\partial w_j}{\partial r} \frac{\partial w_k}{\partial r} \frac{\partial w_l}{\partial r} \frac{\partial w_m}{\partial r} \frac{\partial w_n}{\partial r} \frac{\partial w_q}{\partial r} \frac{\partial w_s}{\partial r} \frac{\partial w_t}{\partial r}\, r\, dr \right\}$$

$$= 0. \tag{32}$$

Requiring validity of (32) for any combinations of the virtual coefficients $\hat{a}_t$ yields a nonlinear system of $N_t$ algebraic equations for the unknowns $a_m$, reading as

$$f_t = V_t^P + V_{t\bar{p}} + V_t^P - \sum_{j,k,l=1}^{N_m} a_j\, a_k\, a_l\, M_{jklt}^I$$

$$- \sum_{j,k,l,m,n=1}^{N_m} a_j\, a_k\, a_l\, a_m\, a_n\, M_{jklmnt}^{II}$$

$$- \sum_{j,k,l,m,n,q,s=1}^{N_m} a_j\, a_k\, a_l\, a_m\, a_n\, a_q\, a_s\, M_{jklmnqst}^{III} = 0, \text{ for } t = 1, 3, ..., N_t,$$

$$\tag{33}$$

with

$$M_{jklt}^I = 2\,\pi\,\rho_{m,0}^{2D}\, c_4 \int\limits_0^R \frac{\partial w_j}{\partial r} \frac{\partial w_k}{\partial r} \frac{\partial w_l}{\partial r} \frac{\partial w_t}{\partial r}\, r\, dr, \tag{34}$$

as the stiffness matrix elements associated to deformation amplitudes of third power (see Appendix A, Eq. (A.4), for analytical expressions concerning (34));

$$M_{jklmnt}^{II} = \frac{3}{2}\, \pi\, \rho_{m,0}^{2D}\, c_5 \int\limits_0^R \frac{\partial w_j}{\partial r} \frac{\partial w_k}{\partial r} \frac{\partial w_l}{\partial r} \frac{\partial w_m}{\partial r} \frac{\partial w_n}{\partial r} \frac{\partial w_t}{\partial r}\, r\, dr, \tag{35}$$

as the stiffness matrix elements associated to deformation amplitudes of fifth power (see Appendix A, Eq. (A.5), for analytical expressions concerning (35));

$$M_{jklmnqst}^{III} = \pi\, \rho_{m,0}^{2D}\, c_7 \int\limits_0^R \frac{\partial w_j}{\partial r} \frac{\partial w_k}{\partial r} \frac{\partial w_l}{\partial r} \frac{\partial w_m}{\partial r} \frac{\partial w_n}{\partial r} \frac{\partial w_q}{\partial r} \frac{\partial w_s}{\partial r} \frac{\partial w_t}{\partial r}\, r\, dr, \tag{36}$$

as the stiffness matrix elements associated to deformation amplitudes of seventh power (see Appendix A, Eq. (A.6), for analytical expressions concerning (36));

$$V_t^p = \int\limits_0^R \int\limits_0^{2\pi} p_{L,z}\, w_t\, r\, d\varphi\, dr, \tag{37}$$

as the load vector elements associated to general surface loads acting on the entire membrane, respectively (see Appendix A, Eq. (A.1), for analytical expressions concerning (37), specified for constant and cosine-type loads);

$$V_{t\bar{p}} = \bar{p}_{L,z} \int\limits_0^{R_T} \int\limits_0^{2\pi} w_t\, r\, d\varphi\, dr, \tag{38}$$

as the load vector elements associated to the distributed load acting over the centered circular area of radius $R_T$ (see Appendix A, Eq. (A.2), for analytical expressions concerning (38));

$$V_t^P = P_{L,z}\, w_t |_{r=0}, \tag{39}$$

as the load vector elements associated to single forces acting in the center of the membrane (see Appendix A, Eq. (A.3), for analytical expressions concerning (39)). The corresponding approximative solution for $u_z(r)$ is more accurate for a larger number $N_m$ of included series deflection members.

As regards solving the derived nonlinear multivariate system of Eq. (33), we resort to the iterative Newton–Raphson method [38] being defined as:

$$\mathbf{a}_{i+1} = \mathbf{a}_i - \mathbf{J}^{-1}(\mathbf{a}_i) \cdot \mathbf{f}(\mathbf{a}_i), \tag{40}$$

where vector $\mathbf{a}_i = [a_{1,i}, a_{3,i}, ..., a_{N_m,i}]^T$ contains the unknown amplitudes $a_{m,i}$ for each iteration step $i$; vector $\mathbf{f} = [f_{1,i}, f_{3,i}, ..., f_{N_t,i}]^T$ contains each line $t$ of the nonlinear system of equation according to (33); and $\mathbf{J}$ is the so-called Jacobian matrix as the partial derivative of $\mathbf{f}$ with respect to the amplitudes $\mathbf{a}$. Thus, the elements of the $N_t \times N_j$ Jacobian matrix for iteration step $i$, when specified for (33), read as:
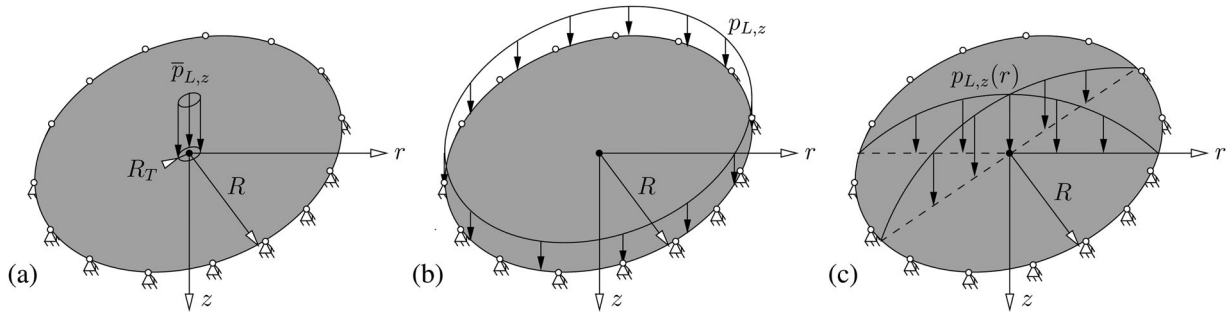
**Figure 3.** Circular graphene membrane with simply supported boundaries and radius $R$, subjected to (a) vertical load $\bar{p}_{L,z}$ distributed over a centered circular area of radius $R_T$, (b) uniform vertical surface load $p_{L,z}$, and (c) non-uniform vertical cosine-type load $p_{L,z}(r)$.
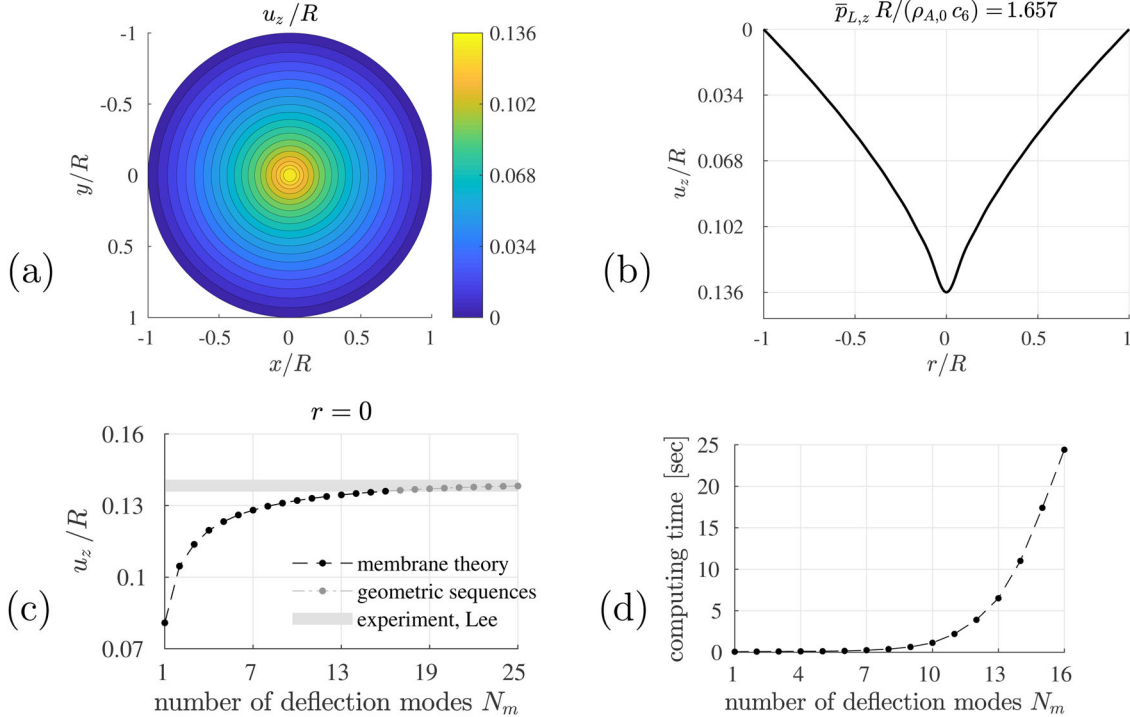


**Figure 4.** Dimensionless deflections $[u_z/R]$ in circular graphene membrane, with simply supported boundary, subjected to a concentrated surface load $\bar{p}_{L,z} \, R/(\rho_{m,0}^{2D} \, c_6) = 1.657$ : (a) deflections in entire membrane, (b) deflections in $r$–$z$-plane, (c) convergence study of the dimensionless deflection located at $r = 0$ as a function of the number of deflection modes $N_m$, and (d) corresponding computing time for results associated to one point of the plate.

$$J_{tj,i} = \frac{\partial f_{t,i}}{\partial a_{j,i}} = -3 \sum_{k,l=1}^{N_m} a_k \, a_l \, M_{jklt}^I - 5 \sum_{k,l,m,n=1}^{N_m} a_k \, a_l \, a_m \, a_n \, M_{jklmnt}^{II}$$

$$- 7 \sum_{k,l,m,n,q,s=1}^{N_m} a_l \, a_l \, a_m \, a_n \, a_q \, a_s \, M_{jklmnqst}^{III}.$$

$$(41)$$

According to the first iteration step, $i = 0$, an initial estimate for the amplitudes $\mathbf{a}_0$ can be directly calculated using a reduced system of equations, including deflection amplitudes up to the third power, namely

$$V_t^p + V_{t\bar{p}} + V_t^P - \sum_{j,k,l=1}^{N_m} a_{j,0} \, a_{k,0} \, a_{l,0} \, M_{jklt}^I = 0,$$

$$(42)$$

for $t = 1, 3, ..., N_t$.

Based on the initial estimate $\mathbf{a}_0$, the Newton–Raphson iteration process (40) is repeated until convergence is reached.

## 4. Application to circular graphene membranes and validation by means of AFM experiments

The structural problem (33)–(39) is now applied to the analysis of a free-standing circular graphene membrane of $R = 500$ nm radius, simply supported at its boundary. In the following, this membrane is subjected to different axisymmetric mechanical loads as constant and cosine-type loads $p_{L,z}(r)$ over the entire membrane, respectively, as well as distributed loads $\bar{p}_{L,z}$ over a circular area of radius $R_T$ (see Figure 3), each of them resulting in a force of $F = 500$ nN. Corresponding results will be presented in a dimensionless way, which does not only comprise the actual deformations arising from the aforementioned material, structural, and loading characteristics, but which reflects infinitely many additional problems which are associated with different membrane radii and different mechanical loads. In more detail, we consider a dimensional analysis [40] of the deflection function (28) arising from the solution of (33), together
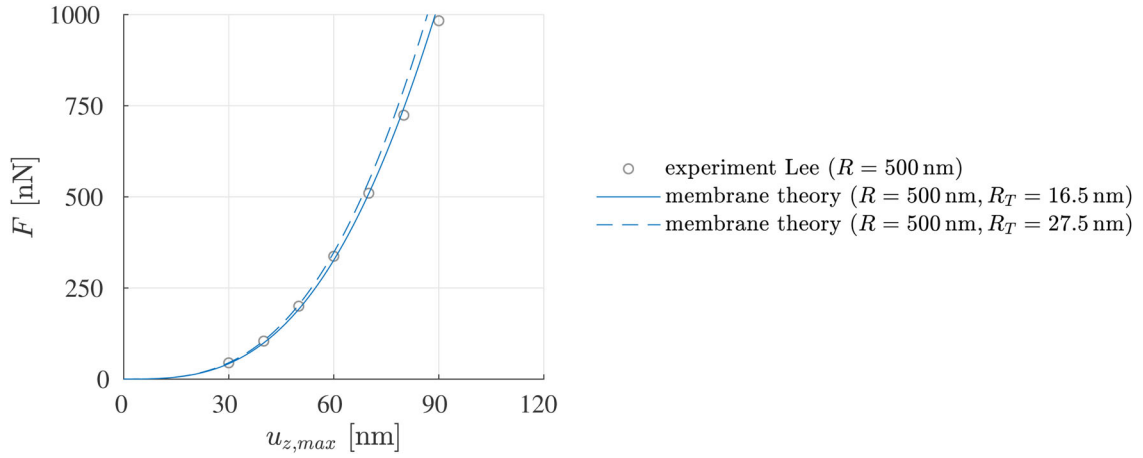
**Figure 5.** Validation of series-based solution procedure (33) according to Example 1 by experimental measurements, as provided by Lee et al. [3] using AFM nanoindentation.

with (34)–(39). This yields the following dimensionless relations

$$\frac{u_z}{R} = \frac{u_z}{R}\left(\frac{r}{R}, \frac{R_T}{R}, \frac{c_3}{c_4}, \frac{c_5}{c_4}, \frac{c_7}{c_4}, \frac{c_{13}}{c_4}, \frac{p_{L,z}\,R}{\rho_{m,0}^{2D}\,c_4}, \frac{\bar{p}_{L,z}\,R}{\rho_{m,0}^{2D}\,c_4}\right). \quad (43)$$

Eq. (43) elucidates that the basic dimensionless functions $[u_z/R]$ depend on geometrical characteristics, in-plane stiffness constants of graphene [34], and dimensionless quantities related to mechanical loadings, so as to deliver dimensionless quantities related to deflections. These relations, depicted in the format of $[u_z/R](r/R = R_T/R = c_3/c_4 = c_5/c_4 = c_7/c_4 = c_{13}/c_4 = p_L, \quad z\,R/(\rho_{m,0}^{2D}\,c_4) = \bar{p}_L, z\,R/(\rho_{m,0}^{2D}\,c_4) = \text{constant})$ in Figures 4, 6, and 7, are valid for any rescaling $R \to \lambda R$, once $r \to \lambda r$, $R_T \to \lambda R_T$, $p_{L,z} \to p_{L,z}/\lambda$, and $\bar{p}_{L,z} \to \bar{p}_{L,z}/\lambda$.

### 4.1. Example 1/validation: Circular graphene membrane subjected to a concentrated load

The circular membrane of radius $R = 500\,\text{nm}$ is subjected to a vertical load $\bar{p}_{L,z}$, which is distributed over the centered circular area of radius $R_T = 16.5\,\text{nm}$, see Figure 3(a). This concentrated load represents the AFM tip used to indent the graphene membrane in the experiment by Lee et al. [3]. In this context, a circular graphene membrane of radius $R = 500\,\text{nm}$ is subjected to the indenter tip, representing a resulting force $F$ acting on a circular area of radius $R_T$ of 16.5 nm and 27.5 nm, respectively. The relation between the Eulerian loading area $dS$ and the Lagrangian loading area $dS_0$,

$$dS_0\ N_z = \frac{dS}{\det \mathbf{F}}\ n_z, \quad (44)$$

results in equivalent loading areas of the indenter, $dS_0 = dS$, when considering $\det \mathbf{F} = 1$ according to (13) and (14), as well as a horizontal tangent of the aforementioned tip with outward normals $N_z = n_z = -1$.

The approximative solution for the dimensionless maximum deflection $[u_z/R]$ located at $r = 0$ can be regarded as converged once $N_m = 16$ series members are employed,

see Figure 4(c). With Matlab version R2012b [41] running on a computer AMD Phenom(tm) II X6 1090 T with 8 GB RAM, this related to 24.4 s computing time, see Figure 4(d). Considering corresponding fields, the maximal deflections occur at the center of the membrane, see Figure 4(a)–(b).

For validation of the obtained structural problem according to (33)–(39), the resulting deflections stemming from the concentrated load are transferred to force–displacement curves up to a force $F$ of 1000 nN. Those curves are then compared to the aforementioned measurements by Lee et al. [3] performed with an atomic force microscope (AFM), see Figure 5. Maximum differences between experimental measurements and series-based results of the deflections $u_{z,max}$ are as low as 0.27% for $F = 500\,\text{nN}$, and 1.44% for $F = 1000\,\text{nN}$.
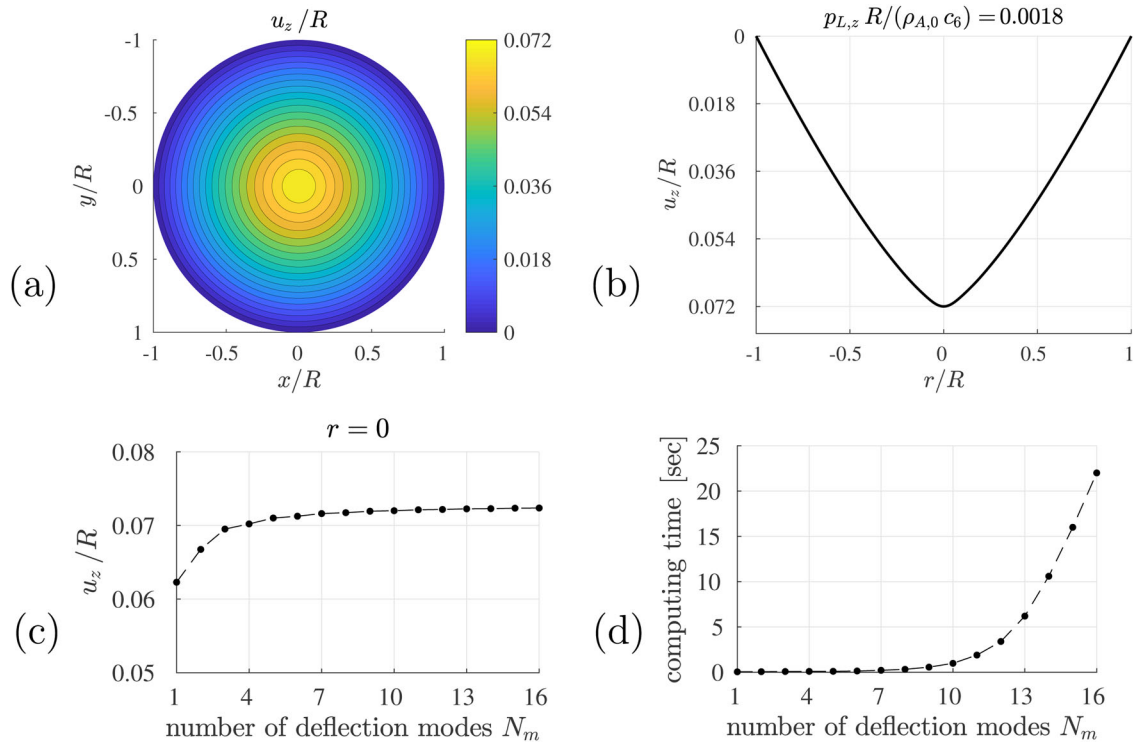
### 4.2. Example 2: Circular graphene membrane subjected to an uniform surface load

The membrane is subjected to an uniform surface load $p_{L,z}(r) = \text{constant} = p_{L,z}$, representing the deadload of a graphene membrane for example, see Figure 3(b). The approximative solution for the dimensionless maximum deflection $[u_z/R]$ at the membrane's center can be regarded as converged once $N_m = 7$ series members are employed, see Figure 6(c). With Matlab version R2012b running on a computer AMD Phenom(tm) II X6 1090 T with 8 GB RAM, this related to 0.2 s computing time, see Figure 6(d). Considering corresponding fields, the maximal deflections occur at the center of the membrane, see Figures 6(a)–(b).
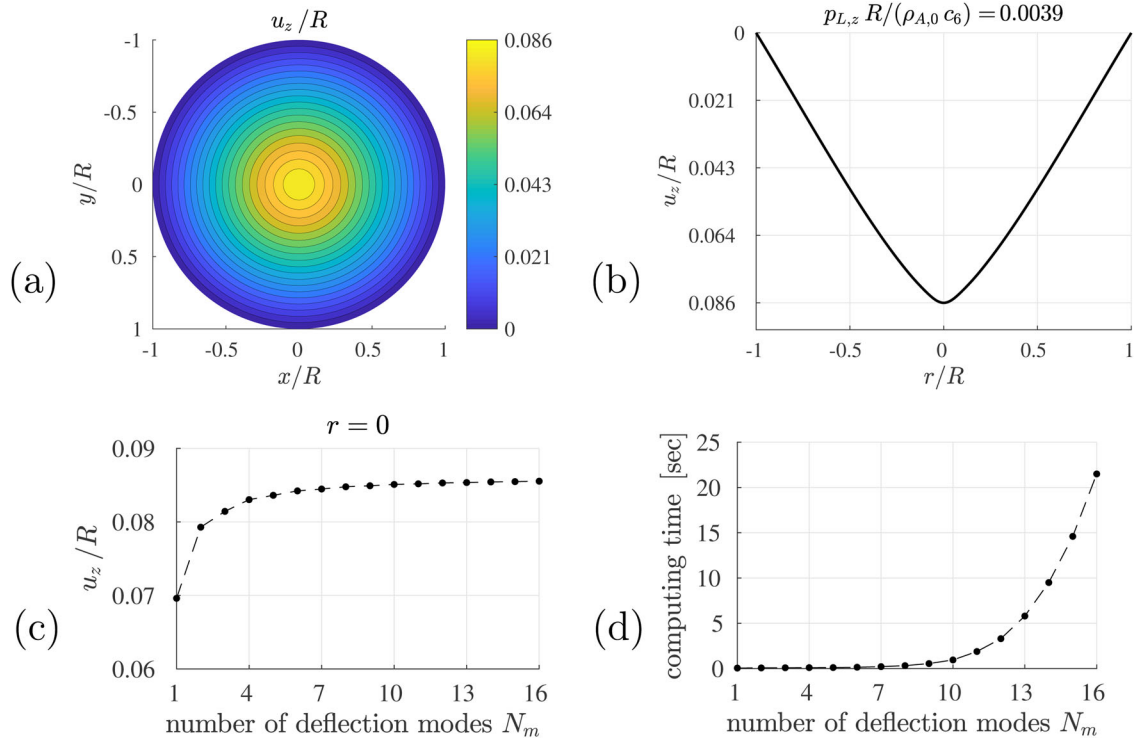
### 4.3. Example 3: Circular graphene membrane subjected to a cosine-type surface load

The membrane is subjected to a cosine-type surface load $p_{L,z}(r) = p_{L,z}\cos{(r\,\pi/(2\,R))}$, representing an external pressure for example, see Figure 3(c). The approximative solution for the dimensionless deflection $[u_z/R]$ at the membrane's center can be regarded as converged once

**Figure 6.** Dimensionless deflections $[u_z/R]$ in circular graphene membrane, with simply supported boundary, subjected to constant surface load $p_{L,z}\ R/(\rho_{m,0}^{2D}\ c_6) = 0.0018$ : (a) deflections in entire membrane, (b) deflections in $r$–$z$-plane, (c) convergence study of the dimensionless deflection located at $r = 0$ as a function of the number of deflection modes $N_m$, and (d) corresponding computing time for results associated to one point of the plate.



**Figure 7.** Dimensionless deflections $[u_z/R]$ in circular graphene membrane, with simply supported boundary, subjected to a cosine-type surface load $p_{L,z}\ R/(\rho_{m,0}^{2D}\ c_6) = 0.0039$ : (a) deflections in entire membrane, (b) deflections in $r$–$z$-plane, (c) convergence study of the dimensionless deflection located at $r = 0$ as a function of the number of deflection modes $N_m$, and (d) corresponding computing time for results associated to one point of the plate.

$N_m = 8$ series members are employed, see Figure 7(c). With Matlab version R2012b running on a computer AMD Phenom(tm) II X6 1090 T with 8 GB RAM, this related to 0.3 s computing time, see Figure 7(d). Considering corresponding fields, the maximal deflections occur at the center of the membrane, see Figure 7(a)–(b).

## 5. Conclusion

The PVP, with rigorous discrimination of internal versus external forces, was applied to the problem of a circular suspended graphene membrane, simply supported at its boundary, and subjected to different axisymmetric mechanical loads. As regards material behavior of graphene, the DFT-based hyperelastic material model [34] was used, and the resulting Fourier series-based nonlinear algebraic system of equations was solved by the iterative Newton–Raphson method. The aforementioned solution procedure also appears as an efficient and computational fast method for modeling specific mechanical problems of graphene membranes. The numerical results are validated by experimental measurements as presented by Lee et al. [3] using AFM nanoindentation, being in good agreement up to large deformations. We regard this as an interesting example for energetically consistent formulations appearing as the basis for particularly relevant and reliable solutions to the growing field of the structural mechanics of graphene. Such an energetically consistent theory is comparable to other nonlinear problems regarding large deformations as the analyses of laminated composite beams using the principle of virtual work and a finite element approximation in a total Lagrangian manner [42]; of inflated circular hyperelastic membranes based on the variational method including a Mooney–Rivlin strain energy [43]; and of the nonlinear vibration response of a neo-Hookean membrane obtained by means of the Galerkin method [44].

## Nomenclature

| | |
|---|---|
| $\mathbf{a}_i$ | vector containing amplitudes $a_{m,i}$ for each iteration step $i$ associated to Newton–Raphson method |
| $a_m$ | Fourier coefficient of deflection approximation |
| $\hat{a}_t$ | Fourier coefficient in approximation of virtual velocity |
| $c_i$ | DFT-based fitting coefficients for hyperelastic material model |
| $\hat{\mathbf{d}}$ | virtual Eulerian strain rate |
| $\mathbf{e}_r, \mathbf{e}_\varphi, \mathbf{e}_z$ | base vectors of cylindrical coordinate system |
| $\mathbf{E}$ | Green–Lagrange strain tensor |
| $E_{rr}$ | normal component of $\mathbf{E}$ in the $r$-direction |
| $\hat{\mathbf{E}}$ | virtual Green–Lagrange strain rate |
| $\hat{E}_{rr}$ | normal component of $\hat{\mathbf{E}}$ in the $r$-direction |
| $\mathbf{f}$ | volume force vector |
| $\mathbf{f}^{NR}$ | vector containing functions $f_t^{NR}$ associated to Newton–Raphson method |
| $f_t^{NR}$ | multivariate function of the nonlinear system of equations |
| $\mathbf{F}$ | deformation gradient |
| $F_{rr}$ | normal component of $\mathbf{F}$ in the $r$-direction |
| $F_{\varphi\varphi}$ | normal component of $\mathbf{F}$ in the $\varphi$-direction |
| $F_{zz}$ | normal component of $\mathbf{F}$ in the $z$-direction |
| $F_{zr}$ | shear component of $\mathbf{F}$ in the $r$–$z$-plane |
| $h$ | effective thickness of graphene |
| $i$ | index of summation/of vector component |
| $I_1, I_3$ | principal invariants of the strain and structural tensor |
| $\mathbf{J}$ | Jacobian matrix associated to Newton–Raphson method |
| $J_{tj,i}$ | elements of $\mathbf{J}$ for each iteration step $i$ |
| $j$ | index of summation/of vector component |
| $k$ | index of summation/of vector component |
| $l$ | index of summation/of vector component |
| $m$ | index of summation/of vector component |
| $M_{jklt}^I$ | "stiffness matrix element" associated to deformation amplitudes of third power |
| $M_{jklmnt}^{II}$ | "stiffness matrix element" associated to deformation amplitudes of fifth power |
| $M_{jklmnt}^{III}$ | "stiffness matrix element" associated to deformation amplitudes of seventh power |
| $n$ | index of summation/of vector component |
| $\mathbf{n}$ | outward normal vector onto the boundaries of deformed continuum |
| $\mathbf{N}$ | outward normal vector onto the boundaries of undeformed membrane |
| $n_{L,rr}$ | internal normal force per unit length in the $r$-direction |
| $N_m$ | number of Fourier series members approximating the deflection |
| $N_t$ | number of Fourier series members approximating the virtual velocity |
| $P_{L,z}$ | single force acting in vertical direction ($z$) |
| $\bar{p}_{L,z}$ | vertical surface load per unit area, acting over specific circular area |
| $p_{L,z}$ | vertical surface load per unit area, acting over entire membrane |
| PVP | principle of virtual power |
| $\mathcal{P}^{ext}$ | virtual power of external forces |
| $\mathcal{P}^{int}$ | virtual power of internal forces |
| $q$ | index of summation/of vector component |
| $r$ | radial coordinate of the cylindrical coordinate system |
| $R$ | radius of the membrane |
| $R_T$ | radius of the surface load $\bar{p}_{L,z}$ |
| $\mathbf{S}$ | derivative of the principal invariant $I_3$ with respect to $\mathbf{E}$ |
| $S_{rr}$ | component of $\mathbf{S}$ in the $r$-direction, characterizing graphene's anisotropic material behavior |
| $s$ | index of summation/of vector component |
| $t$ | index of summation/of vector component |
| $\mathbf{T}$ | traction vector |
| $\mathbf{u}$ | displacement vector |
| $\hat{\mathbf{u}}$ | virtual displacement vector |
| $u_z$ | deflection of the membrane |
| $\hat{u}_z$ | virtual deflection of the membrane |
| $\hat{\mathbf{v}} = \hat{\mathbf{u}}\dot{}$ | virtual velocity vector |
| $v_z$ | component of $\hat{\mathbf{v}}$ in the $z$-direction |
| $V_t^p$ | "load vector element" associated to surface load acting on entire membrane |
| $V_{t\bar{p}}$ | "load vector element" associated to surface load acting on circular area |
| $V_t^P$ | "load vector element" associated to single force |
| $w_m$ | $m$th deflection mode associated to 2D Fourier series |
| $\mathbf{x}$ | location vector throughout the deformed membrane |
| $\mathbf{X}$ | location vector throughout the undeformed membrane |
| $z$ | vertical coordinate of the cylindrical coordinate system |
| $\beta_1, \beta_2, \beta_3$ | scalar functions of the hyperelastic material model for graphene |
| $\lambda$ | scaling factor |
| $\boldsymbol{\pi}$ | second Piola–Kirchhoff stress tensor |
| $\pi_{rr}$ | normal component of $\boldsymbol{\pi}$ in the $r$-direction |
| $\pi_{rz}$ | shear component of $\boldsymbol{\pi}$ in the $r$–$z$-plane |
| $\pi_{zz}$ | normal component of $\boldsymbol{\pi}$ in the $z$-direction |
| $\pi_{rr}^{2D}$ | normal component of 2D second Piola–Kirchhoff stress tensor |
| $\rho_{m,0}^{2D}$ | initial mass density per area of graphene |
| $\boldsymbol{\sigma}$ | Cauchy stress tensor |
| $\sum$ | summation operator |
| $\varphi$ | azimuth of the cylindrical coordinate system |

## References

[1] A.A. Balandin, et al., Superior thermal conductivity of single-layer graphene, Nano Lett., vol. 8, no. 3, pp. 902–907, 2008. DOI: 10.1021/nl0731872.

[2] K.I. Bolotin, et al., Ultrahigh electron mobility in suspended graphene, Solid State Commun., vol. 146, no. 9–10, pp. 351–355, 2008. DOI: 10.1016/j.ssc.2008.02.024.

[3] C. Lee, X. Wei, J.W. Kysar, and J. Hone, Measurement of the elastic properties and intrinsic strength of monolayer graphene, Science, vol. 321, no. 5887, pp. 385–388, 2008. DOI: 10.1126/science.1157996.

[4] A.H. Castro Neto, F. Guinea, N.M.R. Peres, K.S. Novoselov, and A.K. Geim, The electronic properties of graphene, Rev. Mod. Phys., vol. 81, no. 1, pp. 109–155, 2009. DOI: 10.1103/RevModPhys.81.109.

[5] C.N. Lau, W. Bao, and J. Velasco, Properties of suspended graphene membranes, Materialstoday, vol. 15, no. 6, pp. 238–245, 2012. DOI: 10.1016/S1369-7021(12)70114-1.

[6] M. Neek-Amal and F.M. Peeters, Continuum-molecular modelling of graphene, Phys. Rev. B, vol. 81, no. 23, pp. 235421, 2010. DOI: 10.1103/PhysRevB.81.235421.

[7] T.-H. Fang, T.H. Wang, J.-C. Yang, and Y.-J. Hsiao, Mechanical characterization of nanoindented graphene via molecular dynamics simulations, Nanoscale Res. Lett., vol. 6, pp. 481, 2011. DOI: 10.1186/1556-276X-6-481.

[8] A. Shakouri, T.Y. Ng, and R.M. Lin, A new rebo potential based atomistic structural model for graphene sheets, Nanotechnology, vol. 22, no. 29, pp. 295711, 2011. DOI: 10.1088/0957-4484/22/29/295711.

[9] K. Samadikhah, R. Larsson, F. Bazooyar, and K. Bolton, Continuum-molecular modelling of graphene, Comput. Mater. Sci., vol. 53, no. 1, pp. 37–43, 2012. DOI: 10.1016/j.commatsci.2011.09.018.

[10] A. Sakhaee-Pour, M.T. Ahmadian1, and R. Naghdabadi, Vibrational analysis of single-layered graphene sheets, Nanotechnology, vol. 19, no. 8, pp. 085702, 2008. DOI: 10.1088/0957-4484/19/8/085702.

[11] A. Sakhaee-Pour, Elastic buckling of single-layered graphene sheet, Comput. Mater. Sci., vol. 45, no. 2, pp. 266–270, 2009. DOI: 10.1016/j.commatsci.2008.09.024.

[12] S. Rouhi and R. Ansari, Atomistic finite element model for axial buckling and vibration analysis of single-layered graphene sheets, Physica E, vol. 44, no. 4, pp. 764–772, 2012. DOI: 10.1016/j.physe.2011.11.020.

[13] A.J. Gil, S. Adhikari, F. Scarpa, and J. Bonet, The formation of wrinkles in single-layer graphene sheets under nanoindentation, J. Phys.: Condens. Matter., vol. 22, no. 14, pp. 145302, 2010. DOI: 10.1088/0953-8984/22/14/145302.

[14] F. Scarpa, S. Adhikari, A.J. Gil, and C. Remillat, The bending of single layer graphene sheets: the lattice versus continuum approach, Nanotechnology, vol. 21, no. 12, pp. 125702, 2010. DOI: 10.1088/0957-4484/21/12/125702.

[15] R. Larsson and K. Samadikhah, Atomistic continuum modeling of graphene membranes, Comput. Mater. Sci., vol. 50, no. 5, pp. 1744–1753, 2011. DOI: 10.1016/j.commatsci.2011.01.006.

[16] M. Xu, J.T. Paci, J. Oswald, and T. Belytschko, A constitutive equation for graphene based on density functional theory, Int. J. Solids Struct., vol. 49, no. 18, pp. 2582–2589, 2012. DOI: 10.1016/j.ijsolstr.2012.05.019.

[17] M. Xu, A. Tabarraei, J.T. Paci, J. Oswald, and T. Belytschko, A coupled quantum/continuum mechanics study of graphene fracture, Int. J. Fract., vol. 173, no. 2, pp. 163–173, 2012. DOI: 10.1007/s10704-011-9675-x.

[18] X. Wei and J.W. Kysar, Experimental validation of multiscale modeling of indentation of suspended circular graphene membranes, Int. J. Solids Struct., vol. 49, no. 22, pp. 3201–3209, 2012. DOI: 10.1016/j.ijsolstr.2012.06.019.

[19] S. Jiang, S. Shi, and X. Wang, Nanomechanics and vibration analysis of graphene sheets via a 2D plate model, J. Phys. D: Appl. Phys., vol. 47, no. 4, pp. 045104, 2014. DOI: 10.1088/0022-3727/47/4/045104.

[20] S. Seifoori and H. Hajabdollahi, Impact behavior of single-layered graphene sheets based on analytical model and molecular dynamics simulation, Appl. Surf. Sci., vol. 351, pp. 565–572, 2015. DOI: 10.1016/j.apsusc.2015.05.114.

[21] R. Ghaffari, T.X. Duong, and R.A. Sauer, A new shell formulation for graphene structures based on existing ab-initio data, Int. J. Solids Struct., vol. 135, pp. 37–60, 2018. DOI: 10.1016/j.ijsolstr.2017.11.008.

[22] M. Sadeghi and R. Naghdabadi, Nonlinear vibrational analysis of single-layer graphene sheets, Nanotechnology, vol. 21, no. 10, pp. 105705, 2010. DOI: 10.1088/0957-4484/21/10/105705.

[23] J.R. Mianroodi, S.A. Niaki1, R. Naghdabadi, and M. Asghari, Nonlinear membrane model for large amplitude vibration of single layer graphene sheets, Nanotechnology, vol. 22, no. 30, pp. 305703, 2011. DOI: 10.1088/0957-4484/22/30/305703.

[24] C.G. Wang, L. Lan, Y.P. Liu, H.F. Tan, and X.D. He, Vibration characteristics of wrinkled single-layered graphene sheets, Int. J. Solids Struct., vol. 50, no. 10, pp. 1812–1823, 2013. DOI: 10.1016/j.ijsolstr.2013.02.002.

[25] P. Germain, Mécanique des milieux continus [Continuum Mechanics], C. R. Acad. Sc. Paris., vol. 274, no. Série A, pp. 1051–1055, 1972. in French.

[26] P. Germain, La méthode des puissances virtuelles en mécanique des milieu continus [The principle of virtual power in solid mechanics], J. Méc., vol. 12, no. 2, pp. 235–274, 1973. in French.

[27] P. Germain, The method of virtual power in continuum mechanics. Part 2: microstructure, SIAM J. Appl. Math., vol. 25, no. 3, pp. 556–575, 1973. DOI: 10.1137/0125053.

[28] P. Germain, Q.S. Nguyen, and P. Suquet, Continuum thermo-dynamics, Trans. ASME, vol. 50, no. 4b, pp. 1010–1020, 1983. DOI: 10.1115/1.3167184.

[29] G.A. Maugin, The method of virtual power in continuum mechanics: application to coupled fields, Acta Mech., vol. 35, no. 1–2, pp. 1–70, 1980. DOI: 10.1007/BF01190057.

[30] G.A. Maugin, The principle of virtual power: from eliminating metaphysical forces to providing an efficient modelling tool, Contin. Mech. Thermodyn., vol. 25, no. 2–4, pp. 127–146, 2013. DOI: 10.1007/s00161-011-0196-7.

[31] M. Touratier, An efficient standard plate theory, Int. J. Eng. Sci., vol. 29, no. 8, pp. 901–916, 1991. DOI: 10.1016/0020-7225(91)90165-Y.

[32] J. Salençon, Handbook of Continuum Mechanics, Springer-Verlag, Berlin, 2001.

[33] R. Höller, et al., Rigorous amendment of Vlasov's theory for thin elastic plates on elastic Winkler foundations, based in the Principle of Virtual Power, Eur. J. Mech./A Solids., vol. 73, pp. 449–482, 2019. DOI: 10.1016/j.euromechsol.2018.07.013.

[34] R. Höller, V. Smejkal, F. Libisch, and C. Hellmich, Energy land-scapes of graphene under general deformations: DFT-to-hypere-lasticity upscaling, Int. J. Eng. Sci. (in press), 2020. DOI: 10.1016/j.ijengsci.2020.103342

[35] P. Hohenberg and W. Kohn, Inhomogeneous electron gas, Phys. Rev., vol. 136, no. 3B, pp. B864–B871, 1964. DOI: 10.1103/PhysRev.136.B864.

[36] W. Kohn, and L.J. Sham, Self-consistent equations including exchange and correlation effects, Phys. Rev., vol. 140, no. 4A, pp. A1133–A1138, 1965. DOI: 10.1103/PhysRev.140.A1133.

[37] C. L. M. H. Navier, Extrait des recherches sur la flexion des plans élastiques [Excerpt from research on bending of elastic planes], Bull. Soc. Philomath, Paris, vol. 5, pp. 92–102, 1823. in French.

[38] J.M. Ortega and W.C. Rheinboldt, Iterative Solution of Nonlinear Equations in Several Variables (Classics in Applied Mechanics), SIAM, Philadelphia, PA, 2000.

[39] G. Borino and C. Polizzotto, A method to transform a nonlocal model into a gradient one within elasticity and plasticity, Eur. J. Mech. A Solids, vol. 46, pp. 30–41, 2014. DOI: 10.1016/j.euromechsol.2014.01.004.

[40] G.I. Barenblatt, Scaling, Self-Similarity, and Intermediate Asymptotics, 1st ed., Cambridge University Press, Cambridge, England, 1996.

[41] Inc Mathworks. *Matlab*. 1 Apple Hill Drive, Natick, MA 01760-2098, USA, R2012b edition, 2012.

[42] A. Pagani and E. Carrera, Large-deflection and post-buckling analyses of laminated composite beams by Carrera unified formulation, Compos. Struct., vol. 170, pp. 40–52, 2017. DOI: 10.1016/j.compstruct.2017.03.008.

[43] A. Patil and A. DasGupta, Finite inflation of an initially stretched hyperelastic circular membrane, Eur. J. Mech. A/Solids, vol. 41, pp. 28–36, 2013. DOI: 10.1016/j.euromechsol.2013.02.007.

[44] P.B. Gonçalves, R.M. Soares, and D. Pamplona, Nonlinear vibrations of a radially stretched circular hyperelastic membrane, J. Sound Vib., vol. 327, no. 1–2, pp. 231–248, 2009. DOI: 10.1016/j.jsv.2009.06.023.

# Appendix A. Stiffness matrix and load vector elements

In order to determine the unknown coefficients $a_m$, we have to solve the system of algebraic equations (33) together with the corresponding stiffness matrix and load vector elements (34)–(39), for the employed trigonometric functions of type $w_m(r)$, see (29). First, we provide the load vector elements for any combinations of $t = 1, 3, ..., N_t$:

(i) Load vector element associated to the constant and cosine-type surface load $p_{L,z}(r)$ acting on the entire membrane:

$$V_t^p = \int_0^R \int_0^{2\pi} p_{L,z} \, w_t \, r \, d\varphi \, dr$$

$$= \begin{cases} p_{L,z} \frac{4R^2\left[\pi t \sin\left(\frac{\pi t}{2}\right) - 2\right]}{\pi t^2} & p_{L,z}(r) = p_{L,z}, \\ p_{L,z} \frac{R^2(\pi^2 - 4)}{2\pi} & \text{for} \quad p_{L,z}(r) = p_{L,z}\cos\left(\frac{r\pi}{2R}\right), \quad t = 1 \\ p_{L,z} \frac{8R^2\left[2t\sin\left(\frac{\pi t}{2}\right) - t^2 - 1\right]}{\pi(t^2-1)^2} & p_{L,z}(r) = p_{L,z}\cos\left(\frac{r\pi}{2R}\right), \quad t \neq 1, \end{cases}$$

(A.1)

(ii) Load vector element associated to the distributed load $\bar{p}_{L,z}$ acting over the centered circular area of radius $R_T$:

$$V_{t\bar{p}} = \bar{p}_{L,z} \int_0^{R_T} \int_0^{2\pi} w_t \, r \, d\varphi \, dr$$

$$= \bar{p}_{L,z} \frac{4R\left[\pi t R_T \sin\left(\frac{\pi t R_T}{2R}\right) - 4R\sin^2\left(\frac{\pi t R_T}{4R}\right)\right]}{\pi t^2}, \quad (A.2)$$

(iii) Load vector element associated to single forces $P_{L,z}$ acting in the center of the membrane:

$$V_t^P = P_{L,z} \, w_t|_{r=0} = P_{L,z}. \quad (A.3)$$

Next, we provide the stiffness matrix elements $M_{jklt}^I, M_{jklmnt}^{II}$, and $M_{jklmnrst}^{III}$, for any combinations of $j, k, l, m, n, q, s$, and $t$ up to the chosen number of 16 deflection modes (with $N_m = 31$) being sufficient for various mechanical loading cases, see Section 4:

1. Stiffness matrix elements associated to deformation amplitudes of third power:

$$M_{jklt}^I = 2\pi \rho_{m,0}^{2D} c_4 \int_0^R \frac{\partial w_j}{\partial r}\frac{\partial w_k}{\partial r}\frac{\partial w_l}{\partial r}\frac{\partial w_t}{\partial r} \, r \, dr$$

$$= \rho_{m,0}^{2D} c_4 \frac{jklt\,\pi^5}{8R^4} \int_0^R \sin\left(\frac{jr\pi}{2R}\right)\sin\left(\frac{kr\pi}{2R}\right)$$

$$\times \sin\left(\frac{lr\pi}{2R}\right)\sin\left(\frac{tr\pi}{2R}\right) r \, dr$$

(A.4)

$$= \frac{\rho_{m,0}^{2D} c_4}{R^2} A_{jklt}^I, \qquad \text{for} \quad j,k,l,t = 1,3,...,31.$$

2. Stiffness matrix elements associated to deformation amplitudes of fifth power:

$$M_{jklmnt}^{II} = \frac{3}{2}\pi\rho_{m,0}^{2D} c_5 \int_0^R \frac{\partial w_j}{\partial r}\frac{\partial w_k}{\partial r}\frac{\partial w_l}{\partial r}\frac{\partial w_m}{\partial r}\frac{\partial w_n}{\partial r}\frac{\partial w_t}{\partial r} \, r \, dr$$

$$= \frac{3}{2}\rho_{m,0}^{2D} c_5 \frac{jklmnt\,\pi^7}{64R^6}$$

$$\times \int_0^R \sin\left(\frac{jr\pi}{2R}\right)\sin\left(\frac{kr\pi}{2R}\right)\sin\left(\frac{lr\pi}{2R}\right)$$

(A.5)

$$\times \sin\left(\frac{mr\pi}{2R}\right)\sin\left(\frac{nr\pi}{2R}\right)\sin\left(\frac{tr\pi}{2R}\right) r \, dr$$

$$= \frac{\rho_{m,0}^{2D} c_5}{R^4} A_{jklmnt}^{II},$$

$$\text{for} \quad j,k,l,m,n,t = 1,3,...,31.$$

3. Stiffness matrix elements associated to deformation amplitudes of seventh power:

$$M_{jklmnqst}^{III} = \rho_{m,0}^{2D}\pi c_7 \int_0^R \frac{\partial w_j}{\partial r}\frac{\partial w_k}{\partial r}\frac{\partial w_l}{\partial r}\frac{\partial w_m}{\partial r}\frac{\partial w_n}{\partial r}\frac{\partial w_q}{\partial r}\frac{\partial w_s}{\partial r}\frac{\partial w_t}{\partial r} \, r \, dr$$

$$= \rho_{m,0}^{2D} c_7 \frac{jklmnqst\,\pi^9}{256R^8}$$

$$\times \int_0^R \sin\left(\frac{jr\pi}{2R}\right)\sin\left(\frac{kr\pi}{2R}\right)\sin\left(\frac{lr\pi}{2R}\right)\sin\left(\frac{mr\pi}{2R}\right)$$

$$\times \sin\left(\frac{nr\pi}{2R}\right)\sin\left(\frac{qr\pi}{2R}\right)\sin\left(\frac{sr\pi}{2R}\right)\sin\left(\frac{tr\pi}{2R}\right) r \, dr$$

$$= \frac{\rho_{m,0}^{2D} c_7}{R^6} A_{jklmnqst}^{III},$$

$$\text{for} \quad j,k,l,m,n,q,s,t = 1,3,...,31.$$

(A.6)

The dimensionless stiffness matrix elements $A_{jklt}^I, A_{jklmnt}^{II}$, and $A_{jklmnqst}^{III}$ are provided in form of an electronic data set for up 16 deflection modes, see Supplementary material. Since the trigonometric functions of form $\sin(jr\pi/(2R))$, appearing in (A.4)–(A.6), are of similar shape, the ordering of the matrix indices can be chosen arbitrarily. Thus, it is sufficient to calculate matrix elements for indices in descending order, $j \geq k \geq l \geq m \geq n \geq q \geq s \geq t$, which then can be used for any other chosen ordering of the indices.[2]

---

[2] For example, one obtains identical results for dimensionless stiffness matrix elements $A_{jklt}^I$ with indices of form $A_{3111}^I = A_{1311}^I = A_{1131}^I = A_{1113}^I$. The same holds for the matrix elements $A_{jklmnt}^{II}$ and $A_{jklmnqst}^{III}$.